

Phase diagram of $\text{Sr}_{1-x}\text{Ba}_x\text{MnO}_3$ as a function of chemical doping, epitaxial strain, and external pressure

Hanghui Chen^{1,2,3,4,5,*} and Andrew J. Millis¹¹*Department of Physics, Columbia University, New York, New York 10027, USA*²*Department of Applied Physics and Applied Mathematics, Columbia University, New York, New York 10027, USA*³*New York University Shanghai, Shanghai 200122, China*⁴*NYU-ECNU Institute of Physics at NYU Shanghai, Shanghai 200062, China*⁵*Department of Physics, New York University, New York 10002, USA*

(Received 21 September 2015; revised manuscript received 16 August 2016; published 3 October 2016)

We use *ab initio* calculations to systematically study the phase diagram of multiferroic $\text{Sr}_{1-x}\text{Ba}_x\text{MnO}_3$ ($0 \leq x \leq 1$) as a function of chemical doping, epitaxial strain, and external pressure. We find that by replacing Sr with Ba in cubic SrMnO_3 and imposing epitaxial strain, the material can be tuned to the vicinity of a first order transition between two multiferroic phases, one antiferromagnetic with a smaller polarization and one ferromagnetic with a larger polarization. A giant effective magnetoelectric coupling and cross-field control (electric field control of magnetism or magnetic field control of polarization) can be achieved in the vicinity of the transition. The dependence of the theoretically computed transition point on the choice of exchange correlation functionals is determined and is found to be non-negligible. We also show that the perovskite structure of BaMnO_3 can be stabilized relative to its hexagonal polymorphs at pressures larger than 20 GPa.

DOI: [10.1103/PhysRevB.94.165106](https://doi.org/10.1103/PhysRevB.94.165106)

I. INTRODUCTION

Searching for multiferroic materials, in particular those simultaneously possessing ferroelectric polarization and ferromagnetic moments with strong coupling between the two order parameters, is currently of great interest [1,2]. Among all single-phase multiferroic materials, perovskite $\text{Sr}_{1-x}\text{Ba}_x\text{MnO}_3$ ($0 \leq x \leq 1$) stands out as a promising candidate for multiferroics in theory [3–8]. Ferroelectricity was theoretically predicted in perovskite BaMnO_3 [9]. It was also predicted [10,11] that under biaxial strain, perovskite SrMnO_3 (a paraelectric antiferromagnet at ambient conditions) becomes a ferroelectric ferromagnet.

In this paper we examine the phase diagram of $\text{Sr}_{1-x}\text{Ba}_x\text{MnO}_3$ ($0 \leq x \leq 1$) as a function of chemical doping, epitaxial strain, and external pressure. We show that by doping cubic SrMnO_3 with an appropriate concentration of Ba and imposing epitaxial strain, the material can be tuned to the vicinity of a first order phase transition between two multiferroic phases, one antiferromagnetic with a smaller polarization and one ferromagnetic with a larger polarization. In the vicinity of the transition point, reasonable electric fields can be used to switch the material between ferromagnetic and antiferromagnetic states, while feasible magnetic fields can change the electrical polarization. However, the critical Ba doping and the critical epitaxial strain strongly depend on exchange correlation functionals. Building on our previous work [12], we compare three different versions of Perdew-Burke-Ernzerhof (PBE) parametrized exchange correlation functionals and show that they make substantially different predictions for the position of the magnetic transition boundary in the phase diagram of Ba doping and epitaxial strain. We focus on the perovskite structure of $\text{Sr}_{1-x}\text{Ba}_x\text{MnO}_3$ to achieve effective magnetoelectric couplings. However, BaMnO_3 can also crystallize in hexagonal polymorph, which is more stable

than the perovskite structure. We show that applying an external pressure of over 20 GPa on BaMnO_3 is a feasible approach to stabilize the more interesting perovskite structure over its hexagonal polymorph.

The rest of this paper is organized as follows. Section II presents the computational details. Section III discusses the phase diagram of perovskite $\text{Sr}_{1-x}\text{Ba}_x\text{MnO}_3$ as a function of chemical doping and estimates the fields required for magnetoelectric cross-field control. Section IV presents the magnetic phase diagram of perovskite SrMnO_3 , $\text{Sr}_{0.5}\text{Ba}_{0.5}\text{MnO}_3$, and BaMnO_3 as a function of strain. Section V studies energetic dependence of perovskite and hexagonal polymorphs of BaMnO_3 on external pressure. We conclude in Sec. VI.

II. COMPUTATIONAL DETAILS

We perform density functional theory calculations [13,14] within the *ab initio* plane-wave approach [15], as implemented in the Vienna *ab initio* simulation package (VASP) [16]. We employ projector augmented wave (PAW) pseudopotentials [17,18]. We use an energy cutoff 600 eV. All the calculations allow for spin polarization to study different types of long-range magnetic orderings. For most calculations, both cell and internal coordinates are fully relaxed until each force component is smaller than 10 meV/Å and stress tensor is smaller than 10 kbars. For the study of strain, the in-plane lattice constants are fixed during atomic relaxation; the internal coordinates and out-of-plane lattice constant are fully relaxed. For the study of pressure, the atomic relaxation is converged to a specific external pressure.

We consider different structures of $\text{Sr}_{1-x}\text{Ba}_x\text{MnO}_3$. A $12 \times 12 \times 10$ Monkhorst-Pack grid is used to sample the Brillouin zone of the simulation cell used in Secs. III and IV to study the perovskite structure. For the hexagonal polymorphs studied in Sec. V, a $10 \times 10 \times 10$ Monkhorst-Pack grid is used. The simulation cells are provided in each section for ease of reading.

*Corresponding author: hanghui.chen@nyu.edu

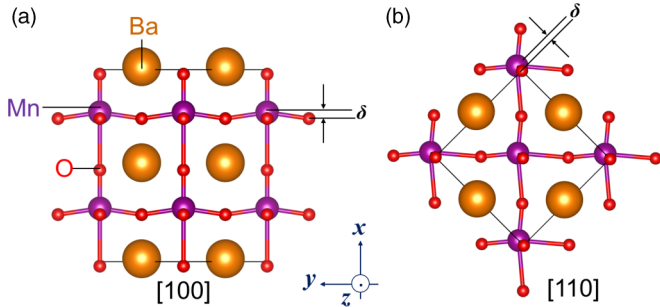


FIG. 1. Atomic structure of perovskite BaMnO_3 . The orange, purple, and red balls are Ba, Mn, and O atoms, respectively. The Mn off-center displacement $\delta_{\text{Mn-O}}$ is formally defined as $\delta_{\text{Mn-O}} = \frac{1}{6} \sum_{i=1}^6 \vec{R}_{\text{Mn-O}_i}$, where $\vec{R}_{\text{Mn-O}_i}$ are the vectors connecting a Mn ion to its six nearest oxygen neighbors. (a) Mn off-center displacement δ along the [100] direction. (b) Mn off-center displacement δ along the [110] direction.

Our recent study shows [12] that different exchange correlation functionals make substantially different predictions for structural and magnetic properties of ferroelectric manganites. By comparing to available experimental data for $\text{Sr}_{0.5}\text{Ba}_{0.5}\text{MnO}_3$ alloy, we establish that charge-density-only generalized gradient approximation with Perdew-Burke-Ernzerhof parametrization [19] plus Hubbard U and Hund's J corrections (PBE+ U + J) [20] and spin-polarized generalized gradient approximation with Perdew-Burke-Ernzerhof parametrization revised for solids (sPBESol) [21] make overall better predictions than the spin-polarized PBE (sPBE) and local spin density approximation (LSDA). In this paper, for most of the results, we use PBE+ U + J and sPBESol. For reference, we also compare PBE+ U + J and sPBESol to sPBE plus effective Hubbard U_{eff} corrections. For the PBE+ U + J method, we use accepted values of $U = 5$ eV and $J = 0.7$ eV for Mn d orbitals unless otherwise specified. This method is implemented in VASP by turning on LDAUTYPE = 4. For the sPBE+ U_{eff} method, we follow previous work [10] and use $U_{\text{eff}} = 1.7$ eV. This method is implemented in VASP by turning on LDAUTYPE = 1.

III. CHEMICAL DOPING

Following our previous work [12], we first use the PBE+ U + J method to examine the Ba-end member compound perovskite BaMnO_3 , considering four different magnetic orderings that are commonly found in manganites: ferromagnetic (F), two-sublattice Néel ordering (G -type), (1, 0, 0) stripe ordering (A -type), and (1, 1, 0) stripe ordering (C -type). Figure 1 shows the atomic structure of perovskite BaMnO_3 . We use a $\sqrt{2} \times \sqrt{2} \times 2$ simulation cell that can accommodate all the above four magnetic orderings. In Fig. 1, δ is the Mn off-center displacement which is along the [100] axis [Fig. 1(a)] and along the [110] axis [Fig. 1(b)].

Figure 2 presents the dependence of the total energy on the Mn off-center displacement $\delta_{\text{Mn-O}}$ for both [100] and [110] directions. The reference energy is that of the G -type antiferromagnet at $\delta_{\text{Mn-O}} = 0$. All the other magnetic states exhibit an energy minimum at $\delta_{\text{Mn-O}} \neq 0$, but the ferromagnetic state is lowest for both directions, and has the largest $\delta_{\text{Mn-O}}$

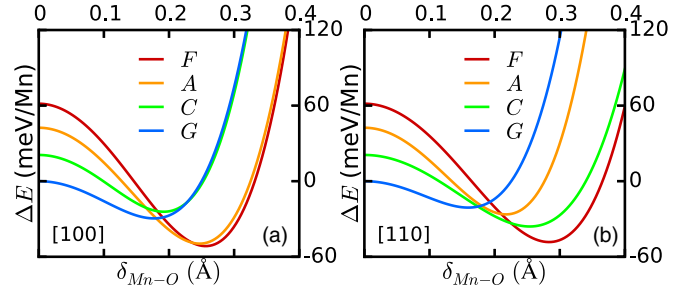


FIG. 2. Change in total energy of perovskite BaMnO_3 as a function of Mn off-center displacement $\delta_{\text{Mn-O}}$ computed using the PBE+ U + J method with $U = 5$ eV and $J = 0.7$ eV for ferromagnetic (F , red curves), A -type antiferromagnetic (A , orange curves), C -type antiferromagnetic (C , green curves), and G -type antiferromagnetic (G , blue curves) states (for the definition of magnetic orderings, see the main text) for (a) along the [100] and (b) along the [110] directions of $\delta_{\text{Mn-O}}$. The zero energy state is chosen as the energy of the G -type antiferromagnetic state at $\delta_{\text{Mn-O}} = 0$. Calculations were first performed using a cubic structure ($\delta_{\text{Mn-O}} = 0$) and a fully relaxed structure, then were interpolated by using intermediate structures.

at the minimum. Interestingly, the energy difference between different magnetic phases depends on the direction of polarization. For $\delta_{\text{Mn-O}}$ along the [110] direction, ferromagnetism is clearly more stable than any of the antiferromagnetic states, while for $\delta_{\text{Mn-O}}$ along the [100] direction, ferromagnetism and A -type antiferromagnetism are extremely close in energy. The near coincidence of energies suggests that for x slightly less than 1, it may be possible to switch the magnetic states by applying an electric field and rotating the orientation of $\delta_{\text{Mn-O}}$.

The results shown in Fig. 2 establish that within the PBE+ U + J method with $U = 5$ eV and $J = 0.7$ eV, perovskite BaMnO_3 is a ferromagnet with strong Mn off-center displacements. Now we consider the evolution of magnetic and ferroelectric states with Ba concentration x in $\text{Sr}_{1-x}\text{Ba}_x\text{MnO}_3$. Figure 3 presents the dependence of the total energy of two magnetic states of $\text{Sr}_{1-x}\text{Ba}_x\text{MnO}_3$ (for $x = 0.0, 0.25, 0.5$,

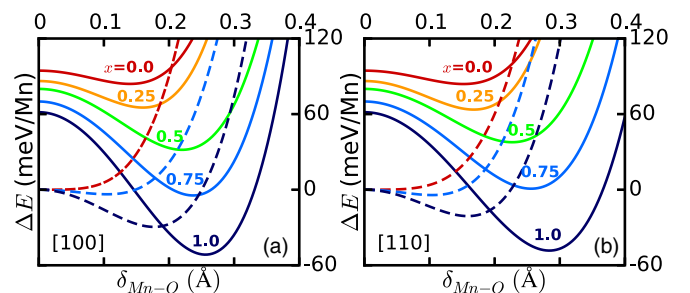


FIG. 3. Total energy of $\text{Sr}_{1-x}\text{Ba}_x\text{MnO}_3$ ($0 \leq x \leq 1$) calculated using the PBE+ U + J method with $U = 5$ eV and $J = 0.7$ eV as a function of Mn off-center displacement $\delta_{\text{Mn-O}}$. The solid lines indicate ferromagnetic ordering and the dashed lines indicate G -type antiferromagnetic ordering. The red, orange, green, blue, and indigo curves correspond to Ba doping of $x = 0, 0.25, 0.5, 0.75$, and 1, respectively. For each x , the zero of energy is chosen as the energy of the G -type antiferromagnet at $\delta_{\text{Mn-O}} = 0$. (a) $\delta_{\text{Mn-O}}$ along the [100] direction; (b) $\delta_{\text{Mn-O}}$ along the [110] direction.

0.75, and 1.0) on the inversion-symmetry-breaking Mn-O displacement $\delta_{\text{Mn-O}}$ along [100] and [110] directions. The figure shows that for both directions of $\delta_{\text{Mn-O}}$, the G -type antiferromagnetic state (which is insulating for all x) has a paraelectric-to-ferroelectric transition as the Ba doping x increases, consistent with previous studies [4–6,9]. We also see that for all x the ferromagnetic state always has a nonzero Mn off-center displacement $\delta_{\text{Mn-O}}$ which is larger than that of antiferromagnetic state at the same x . With increasing Ba doping the energy difference between the ferromagnetic and antiferromagnetic states rapidly decreases and for the parameters $U = 5$ eV and $J = 0.7$ eV used here, a first-order antiferromagnetic-to-ferromagnetic transition occurs around $x = 0.75$ (blue curves), accompanied by an abrupt jump in the Mn off-center displacement. Therefore, in the vicinity of the transition, we can use an external electric field to increase the Mn off-center displacement and change the magnetic ordering, or use an external magnetic field to induce a finite change in Mn off-center displacements. This effective magnetoelectric cross-field control is similar to what is found in epitaxially strained SrMnO_3 [10], indicating that chemical doping is a complementary approach to tuning multiferroic properties.

Based on Fig. 3, we can make some estimation of critical fields required for switching. For physically reasonable parameters $U = 5$ eV and $J = 0.7$ eV, our calculations show that the critical doping x is around 0.75. At $x = 0.75$ and along the [110] direction, the two lowest energy states are G -type antiferromagnetism (G) and ferromagnetism (F). The critical fields are estimated by

$$\mathcal{E}_c(P_F - P_G) \simeq E(F) - E(G), \quad (1)$$

$$\mathcal{H}_c M \simeq E(F) - E(G), \quad (2)$$

where $P_F = 56 \mu\text{C}/\text{cm}^2$ and $P_G = 26 \mu\text{C}/\text{cm}^2$ are electric polarizations calculated using the Berry phase method [22] for ferromagnetic and G -type antiferromagnetic states; M is the on-site magnetic moment, which is about $3 \mu_B$ per Mn; E is the total energy obtained from DFT calculations (the polarization dependence on electric fields is neglected). We find that \mathcal{E}_c is about 42 MV/m and \mathcal{H}_c is about 25 T. While these fields are large, they are experimentally achievable and have been applied to, for example, BaTiO_3 thin films [23]. More importantly, tuning the Ba doping x by a few percent can rapidly reduce these critical fields. Use of other interaction parameters $U = 4$ eV and $J = 0.6$ eV (the smallest U value to stabilize a high-spin state in cubic SrMnO_3 using the $\text{PBE}+U+J$ method [24]) shows that at $x = 1$ we can still switch the two lowest magnetic states by a critical magnetic field of 12 T or switch those two polarizations by an electric field of 30 MV/m. As we see, properly adjusting the Ba doping x can compensate for the uncertainty of U and J parameters in theory.

Our previous works [12,24] show that magnetic properties of transition metal oxides depend on the choice of exchange-correlation functionals. To test whether our prediction of a doping-driven magnetic transition in $\text{Sr}_{1-x}\text{Ba}_x\text{MnO}_3$ is robust to the choice of exchange-correlation potential, we compare three different types of PBE exchange correlation functionals: spin-polarized PBE revised for solids (sPBEsol), charge-

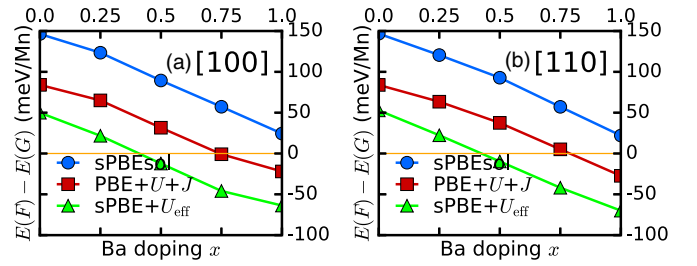


FIG. 4. Energy difference between ferromagnetic state (F) and G -type antiferromagnetic state (G) of $\text{Sr}_{1-x}\text{Ba}_x\text{MnO}_3$ ($0 \leq x \leq 1$) calculated using difference exchange correlation functionals: charge-density-only PBE functional with Hubbard U and Hund's J correction ($\text{PBE}+U+J$) with $U = 5$ eV and $J = 0.7$ eV; spin polarized PBE for solids (sPBEsol) and spin polarized PBE with effective Hubbard U_{eff} correction (sPBE+ U_{eff}). (a) $\delta_{\text{Mn-O}}$ along the [100] direction; (b) $\delta_{\text{Mn-O}}$ along the [110] direction.

density-only PBE plus Hubbard U and Hund's J correction ($\text{PBE}+U+J$), and spin-polarized PBE plus effective U_{eff} correction (sPBE+ U_{eff}) by calculating the energy difference of $\text{Sr}_{1-x}\text{Ba}_x\text{MnO}_3$ between the ferromagnetic and G -type antiferromagnetic states. The comparison is shown in Fig. 4. We find that while $\text{PBE}+U+J$ and sPBE+ U_{eff} predict that there is an antiferromagnetic to ferromagnetic transition as x is increased from 0 to 1 for perovskite $\text{Sr}_{1-x}\text{Ba}_x\text{MnO}_3$, sPBEsol predicts that perovskite $\text{Sr}_{1-x}\text{Ba}_x\text{MnO}_3$ is G -type antiferromagnetic for the whole range of x ($0 \leq x \leq 1$).

We can test the functionals by comparing to experimental data for $\text{Sr}_{0.5}\text{Ba}_{0.5}\text{MnO}_3$ alloy [4]. We find from our previous study [12] that both $\text{PBE}+U+J$ and sPBEsol make good predictions of structural and magnetic properties (better than sPBE, LSDA and $\text{LDA}+U+J$). Hence we cannot definitely predict the ground state magnetic ordering of perovskite BaMnO_3 . However, that doping cubic SrMnO_3 with Ba favors ferromagnetism is a robust result. If the end member perovskite BaMnO_3 were ferromagnetic, then the antiferromagnetic-to-ferromagnetic transition would occur at an intermediate doping x_c , in the vicinity of which an effective giant magnetoelectric coupling can be induced. If perovskite BaMnO_3 were not ferromagnetic, then epitaxial strain may be used to stabilize the ferromagnetic state.

IV. EPITAXIAL STRAIN

Strain engineering has been widely used to induce multiferroic states [11,25]. Lee and Rabe showed [10] that epitaxial strain can induce a ferroelectric-ferromagnetic ground state in an otherwise antiferromagnetic cubic SrMnO_3 with a critical tensile strain of 3.4% (predicted by sPBE plus an effective Hubbard U_{eff} extension, for short sPBE+ U_{eff}). In this section we define the strain λ as

$$\lambda = \frac{a - a_0}{a_0} \times 100\%, \quad (3)$$

where a is a common lattice constant that is imposed on all the magnetic orderings and a_0 is the theoretically calculated lattice constant of the G -type antiferromagnetic state. We note that because we define strain with respect to a particular state (the G -type antiferromagnet), the critical strain depends

both on the energy difference between ferromagnetic and antiferromagnetic states at equilibrium (denoted by δE) and on the difference between equilibrium lattice constant (denoted by $\delta\lambda$). We first compare the predictions of sPBE+ U_{eff} to PBE+ $U+J$ and sPBEsol methods for the phase diagram of strained SrMnO₃. We show that the three methods make substantially different predictions on the critical strain that stabilizes the ferroelectric-ferromagnetic ground state of SrMnO₃.

Next we study the phase diagram of epitaxially strained perovskite Sr_{0.5}Ba_{0.5}MnO₃ alloy and epitaxially strained perovskite BaMnO₃. We show that Ba doping acts like an “effective strain”, so that increasing the Ba concentration in Sr_{1-x}Ba_xMnO₃ can reduce the critical strain that stabilizes the ferromagnetic state. However, just like epitaxially strained SrMnO₃, the critical strain as a function of Ba doping also strongly depends on exchange correlation functionals.

A. Perovskite SrMnO₃

Figure 5 shows the total energies of SrMnO₃ and Mn off-center displacement along the [100] direction under tensile strain. Figures 5(a1) and 5(b1) are calculated using the sPBEsol method. Figures 5(a2) and 5(b2) are calculated using the PBE+ $U+J$ method with $U = 5$ eV and $J = 0.7$ eV. Figures 5(a3) and 5(b3) are calculated using the sPBE+ U_{eff} method with $U_{\text{eff}} = U - J = 1.7$ eV, following Ref. [10]. The **a** panels of Fig. 5 show the total energy of tensile strained SrMnO₃ with different magnetic orderings (F , A , C , and G , as defined in the previous section). We find the predicted critical tensile strain needed to drive a ferromagnetic transition is 6.8% for sPBEsol [not explicitly shown in the Fig. 5(a1)], 4.8% for PBE+ $U+J$, and 3.2% for sPBE+ U_{eff} , respectively. The critical strain for sPBE+ U_{eff} is slightly smaller than that given in Ref. [10] (see [26]). We notice that all three methods predict that with increasing tensile strain, the elastic energy eventually stabilizes the ferromagnetic state over the G -type antiferromagnetic state. However, the strain dependence is substantially different. The difference has two origins. One is the energy difference δE between the ferromagnetic and G -type antiferromagnetic states at equilibrium, which is shown as the dashed vertical lines in the **a** panels of Fig. 5. The other is the difference in equilibrium lattice constants $\delta\lambda$ between the ferromagnetic state and G -type antiferromagnetic state, which is shown as the horizontal lines in the **a** panels of Fig. 5. δE is more important. Increasing δE substantially increases the critical strain. sPBEsol, PBE+ $U+J$, and sPBE+ U_{eff} predict δE to be 149, 83, and 57 meV/Mn, respectively. For a fixed δE , increasing $\delta\lambda$ (within a reasonable range) can reduce the critical strain, because at the same constrained lattice constant, a larger $\delta\lambda$ means that the ferromagnetic state is under smaller strain, thus inducing smaller elastic energy cost. The sPBEsol, PBE+ $U+J$, and sPBE+ U_{eff} methods predict that the equilibrium lattice constant of the ferromagnetic state is 1.4%, 0.5%, and 1.6% larger than that of the G -type antiferromagnetic state. sPBE+ U_{eff} predicts the smallest δE and the largest $\delta\lambda$, the combination of which leads to the smallest critical strain (3.4%). On the other hand, sPBEsol predicts the largest δE , which leads to the largest critical strain (6.8%).

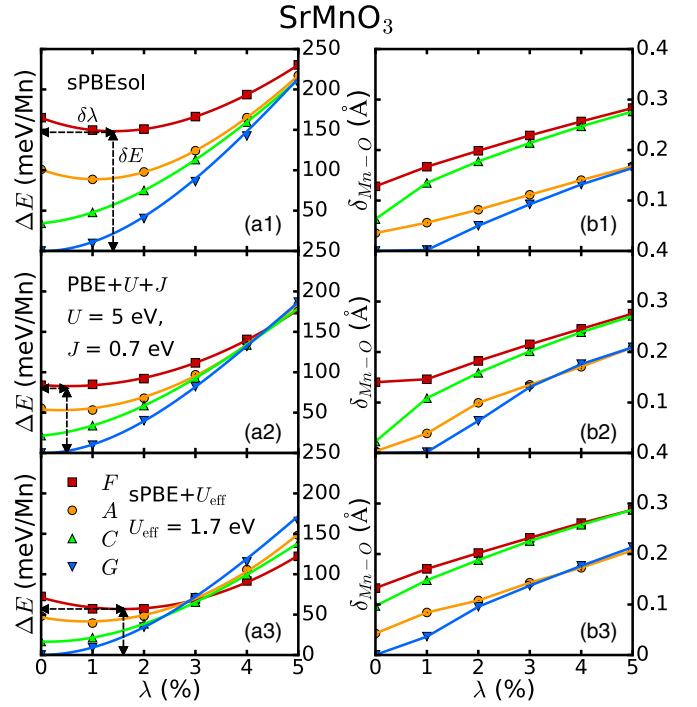


FIG. 5. Perovskite SrMnO₃: (a1) and (b1) using the sPBEsol method. (a1) Total energy for different magnetic states under tensile strain. The zero point is chosen as the total energy of G -type antiferromagnetic state at zero strain. λ is the strain with respect to the equilibrium lattice constant of G -type antiferromagnetic state. (b1) Mn off-center displacement along the [110] direction of SrMnO₃ for different magnetic states under tensile strain. (a2) and (b2) using the PBE+ $U+J$ method with $U = 5$ eV and $J = 0.7$ eV. (a2) same as (a1), (b2) same as (b1). (a3) and (b3) using the sPBE+ U_{eff} method with $U_{\text{eff}} = U - J = 1.7$ eV. (a3) same as (a1), (b3) same as (b1). The red squares and lines are the ferromagnetic state (F). The orange squares and lines are the A -type antiferromagnetic state (A). The green squares and lines are the C -type antiferromagnetic state (C). The blue squares and lines are the G -type antiferromagnetic state (G). The horizontal dashed line denotes $\delta\lambda$, which is the difference in equilibrium lattice constants between F and G orderings. The vertical dashed line denotes δE , which is the equilibrium energy difference between F and G orderings.

The **b** panels of Fig. 5 show the Mn off-center displacement $\delta_{\text{Mn-O}}$ along the [110] direction for strained SrMnO₃. We find that all the three methods yield similar behavior for $\delta_{\text{Mn-O}}$ with sPBE+ U_{eff} predicting a slightly larger displacement than sPBEsol and PBE+ $U+J$, consistent with our previous study [12].

Finally, we briefly discuss the Hubbard U dependence. We study the U dependence using the PBE+ $U+J$ method, but the conclusion also applies to sPBE+ U_{eff} . We study several different values of Hubbard U and compare the results in Fig. 6. As we increase the Hubbard U from 4 to 5 to 6 eV, δE (dashed vertical lines in Fig. 6) is reduced from 103 to 83 to 66 meV/Mn. At the same time, $\delta\lambda$ (dashed horizontal lines in Fig. 6) also decreases from 1.2%, to 0.5% to 0.4%. While a decreasing δE favors the ferromagnetism and a decreasing $\delta\lambda$ disfavors the ferromagnetism, δE is the dominating factor and eventually the critical strain is reduced. Therefore, increasing

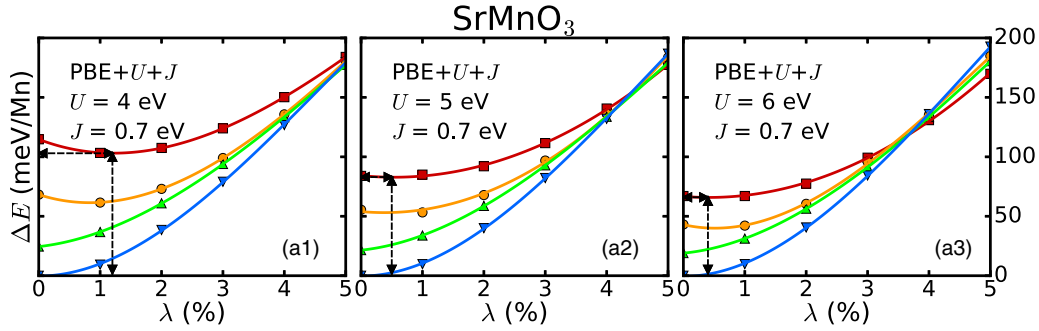


FIG. 6. Calculations of total energies of SrMnO₃ for different magnetic states under tensile strain, using the PBE+*U*+*J* method [(a1) *U* = 4 eV; (a2) *U* = 5 eV; (a3) *U* = 6 eV; for all three cases, *J* = 0.7 eV]. The red squares and lines are the ferromagnetic state (*F*). The orange squares and lines are the *A*-type antiferromagnetic state (*A*). The green squares and lines are the *C*-type antiferromagnetic state (*C*). The blue squares and lines are the *G*-type antiferromagnetic state (*G*). The horizontal dashed line denotes $\delta\lambda$, which is the difference in equilibrium lattice constants between *F* and *G* orderings. The vertical dashed line denotes δE , which is the equilibrium energy difference between *F* and *G* orderings.

U favors the ferromagnetism, which is consistent with the simple picture that a larger *U* suppresses the superexchange and antiferromagnetism, and thus ferromagnetism is favored.

B. Perovskite Sr_{0.5}Ba_{0.5}MnO₃ alloy

In this subsection we study perovskite Sr_{0.5}Ba_{0.5}MnO₃ alloy under epitaxial strain. To simulate cation alloys, we employ a simulation cell with a checkerboard arrangement of Sr-Ba cations (see Fig. 7).

To be consistent with the study of strained SrMnO₃ in the previous subsection, we consider the Mn off-center displacement along the [110] direction and apply tensile strain, which can enhance the [110] polarization. Following the same convention, the biaxial strain λ is defined in Eq. (3). Like SrMnO₃, we also study four common magnetic orderings (*F*, *A*, *C*, *G*) in Sr_{0.5}Ba_{0.5}MnO₃ alloy. The **a** panels of Fig. 8 present the total energy of different magnetic orderings of Sr_{0.5}Ba_{0.5}MnO₃ alloy as a function of tensile strain, using sPBEsol, PBE+*U*+*J*, and sPBE+*U*_{eff}. First we notice that for all three methods, at $\lambda = 0$, the *G*-type antiferromagnetic state has lower energy than the ferromagnetic state. With an increasing lattice constant *a*, the total energy of the *G*-type antiferromagnetic ordering monotonically increases, while

the total energy of the ferromagnetic state first decreases to the minimum at its own equilibrium position and then increases with strain. In particular, we notice that for the sPBE+*U*_{eff} method, the minimum of the ferromagnetic state

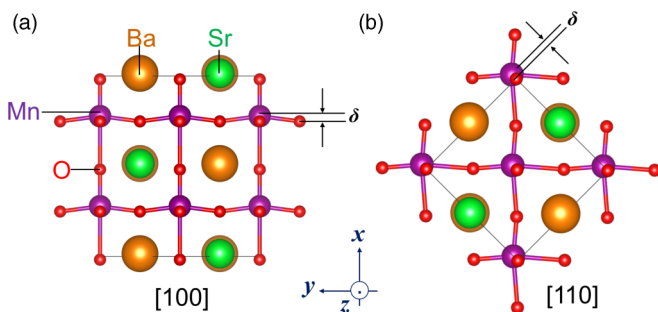


FIG. 7. Atomic structure of perovskite Sr_{0.5}Ba_{0.5}MnO₃. The orange, green, purple, and red balls are Sr, Ba, Mn, and O atoms, respectively. (a) Mn off-center displacement δ along the [100] axis direction. (b) Mn off-center displacement δ along the [110] axis direction. For tensile strain, we focus on Mn off-center displacement δ along the [110] axis direction.

Sr_{0.5}Ba_{0.5}MnO₃

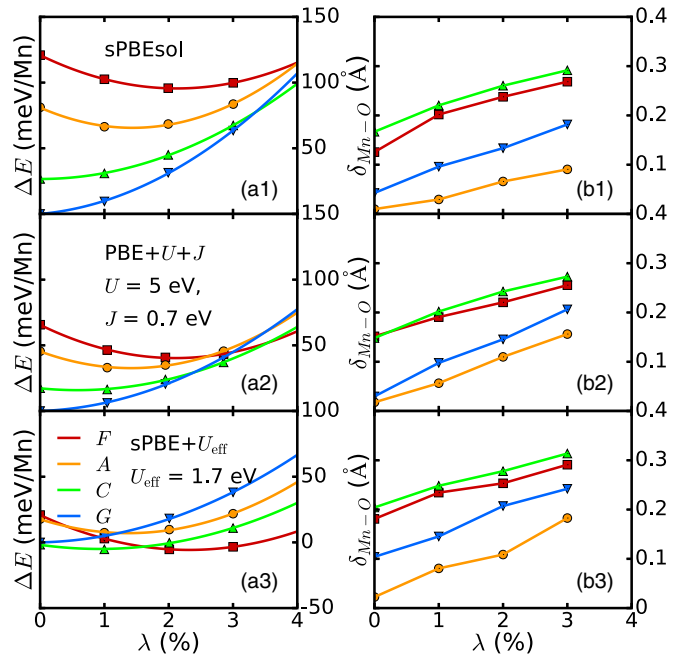


FIG. 8. Perovskite Sr_{0.5}Ba_{0.5}MnO₃: (a1) and (b1) using the sPBEsol method. (a1) Total energy for different magnetic states under tensile strain. The zero point is chosen as the total energy of *G*-type antiferromagnetic state at zero strain. λ is the strain with respect to the equilibrium lattice constant of *G*-type antiferromagnetic state. (b1) Mn off-center displacement along the [110] direction of SrMnO₃ for different magnetic states under tensile strain. (a2) and (b2) using the PBE+*U*+*J* method with *U* = 5 eV and *J* = 0.7 eV. (a2) same as (a1). (b2) same as (b1). (a3) and (b3) using the sPBE+*U*_{eff} method with *U*_{eff} = *U* - *J* = 1.7 eV. (a3) same as (a1). (b3) same as (b1). The red squares and lines are the ferromagnetic state (*F*). The orange squares and lines are the *A*-type antiferromagnetic state (*A*). The green squares and lines are the *C*-type antiferromagnetic state (*C*). The blue squares and lines are the *G*-type antiferromagnetic state (*G*).

is lower than the minimum of the G -type antiferromagnetic state. This means that without any epitaxial strain, sPBE+ U_{eff} predicts that the ground state of the $\text{Sr}_{0.5}\text{Ba}_{0.5}\text{MnO}_3$ alloy is ferromagnetic, which is inconsistent with the experiment [4]. However, sPBEsol and PBE+ $U+J$ predict that the ground state of the $\text{Sr}_{0.5}\text{Ba}_{0.5}\text{MnO}_3$ alloy is G -type antiferromagnetic. Therefore, using sPBEsol and PBE+ $U+J$ methods, we predict that we need a critical tensile strain (5.2% and 3.5%, respectively) to stabilize the ferromagnetic state.

For all three methods, the critical strain is predicted to be smaller than that of pure SrMnO_3 because the presence of Ba increases the Mn off-center displacement and favors the ferromagnetic ordering [10], which acts as an “effective strain.” The **b** panels of Fig. 8 show the Mn off-center displacement $\delta_{\text{Mn-O}}$, which monotonically increases as a function of strain. For each method, at the critical strain, the Mn off-center displacement $\delta_{\text{Mn-O}}$ of the ferromagnetic state exceeds 0.25 Å, which is larger than the Ti off-center displacements of commercially important ferroelectrics BaTiO_3 .

C. Perovskite BaMnO_3

In this subsection we study perovskite BaMnO_3 under epitaxial strain. The simulation cell is shown in Fig. 1. We follow the convention of the previous two subsections. The results are shown in Fig. 9. From the **a** panels of Fig. 9, both PBE+ $U+J$ and sPBE+ U_{eff} predict that without any epitaxial strain, the ground state of perovskite BaMnO_3 is ferromagnetic. However, sPBEsol predict that the ground state of perovskite BaMnO_3 is still G -type antiferromagnetic ordering and 4% tensile strain is needed to stabilize the ferromagnetic state. From the **b** panels of Fig. 9, we find that within a 4% tensile strain, all the three methods predict a robust Mn off-center displacement for the four magnetic orderings investigated.

Finally, we summarize the critical tensile strain for $\text{Sr}_{1-x}\text{Ba}_x\text{MnO}_3$ ($x = 0, 0.5, \text{ and } 1$) calculated with different exchange correlation functionals in Table I. It is evident that for all three methods used here, increasing Ba doping decreases the critical strain that stabilizes the ferromagnetic ordering. For each Ba doping x in $\text{Sr}_{1-x}\text{Ba}_x\text{MnO}_3$, sPBE+ U_{eff} most favors ferromagnetism, while sPBEsol least favors ferromagnetism. This is consistent with Fig. 4.

We also studied the compressive strain (not shown here), which enhances the polarization along the [100] direction. For compressive strain, the magnetic energy dependence on strain and exchange correlation functional is very similar to what we have found for tensile strain.

V. PRESSURE STABILIZATION OF PEROVSKITE BaMnO_3

While our calculations predict that perovskite $\text{Sr}_{1-x}\text{Ba}_x\text{MnO}_3$ has appealing multiferroic properties, a hexagonal polymorph of manganites has lower energy than the perovskite structure [27,28]. However, the perovskite polymorph may be stabilized by pressure [29]. In this section we focus on BaMnO_3 and study the energetics of different polymorphs as a function of pressure. All the results presented are obtained using the PBE+ $U+J$ method ($U = 5$ eV and $J = 0.7$ eV). Other methods, such as sPBEsol and sPBE,

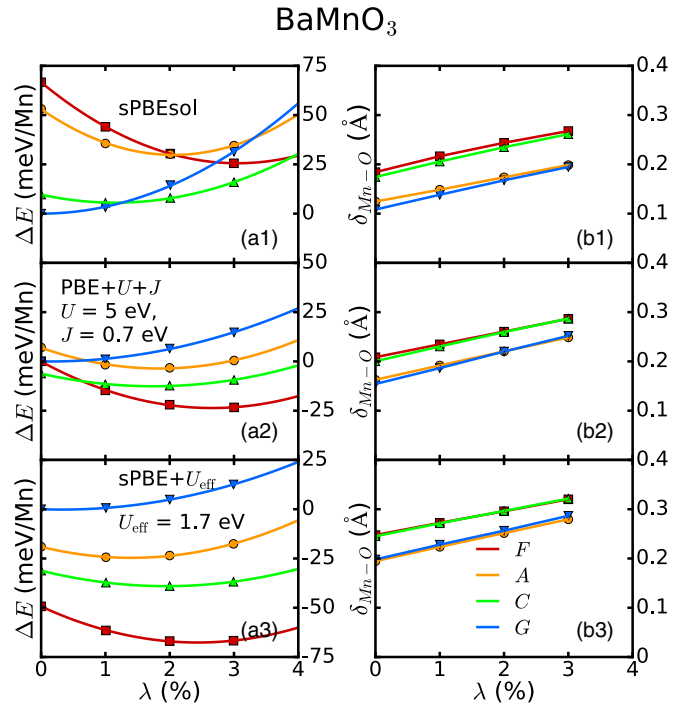


FIG. 9. Perovskite BaMnO_3 : (a1) and (b1) using the sPBEsol method. (a1) Total energy for different magnetic states under tensile strain. The zero point is chosen as the total energy of G -type antiferromagnetic state at zero strain. λ is the strain with respect to the equilibrium lattice constant of G -type antiferromagnetic state. (b1) Mn off-center displacement along the [110] direction of SrMnO_3 for different magnetic states under tensile strain. (a2) and (b2) using the PBE+ $U+J$ method with $U = 5$ eV and $J = 0.7$ eV. (a2) same as (a1). (b2) same as (b1). (a3) and (b3) using the sPBE+ U_{eff} method with $U_{\text{eff}} = U - J = 1.7$ eV. (a3) same as (a1). (b3) same as (b1). The red squares and lines are the ferromagnetic state (F). The orange squares and lines are the A -type antiferromagnetic state (A). The green squares and lines are the C -type antiferromagnetic state (C). The blue squares and lines are the G -type antiferromagnetic state (G).

yield qualitatively consistent conclusions, but with a critical pressure 20% larger in magnitude (see below).

Figure 10 shows the atomic structure of five different polymorphs of BaMnO_3 . Figure 10(a) shows the structure of hexagonal BaMnO_3 with face-sharing MnO_6 oxygen octahedra. This structure is called $2H$. Figure 10(b) is also a hexagonal structure of BaMnO_3 with mixed face-sharing and corner-sharing MnO_6 oxygen octahedra. This structure is

TABLE I. Critical tensile strain that stabilizes ferromagnetic state in $\text{Sr}_{1-x}\text{Ba}_x\text{MnO}_3$ ($0 \leq x \leq 1$), calculated using the sPBEsol, PBE+ $U+J$, and sPBE+ U_{eff} methods. In the PBE+ $U+J$ method, we use $U = 5$ eV and $J = 0.7$ eV. In the sPBE+ U_{eff} method we use $U_{\text{eff}} = 1.7$ eV.

	sPBEsol	PBE+ $U+J$	sPBE+ U_{eff}
SrMnO_3	6.8%	4.8%	3.2%
$\text{Sr}_{0.5}\text{Ba}_{0.5}\text{MnO}_3$	5.2%	3.5%	no strain needed
BaMnO_3	4.0%	no strain needed	no strain needed

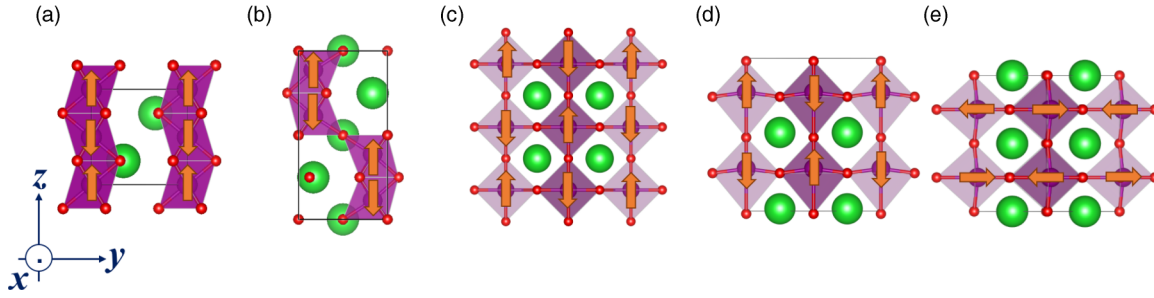


FIG. 10. Five different atomic structures of BaMnO_3 . The green balls are La atoms. The purple cages are MnO_6 . (a) The hexagonal structure with face-sharing MnO_6 oxygen octahedra; (b) the hexagonal structure with mixed face-sharing and corner sharing MnO_6 oxygen octahedra; (c) the cubic perovskite structure with corner-sharing MnO_6 oxygen octahedra; (d) the tetragonal perovskite structure with Mn off-center displacement along the z direction; and (e) the orthorhombic perovskite structure with Mn off-center displacement in the xy plane. The orange arrows indicate spin arrangements in the antiferromagnetic state considered for each structure.

called $4H$. Figure 10(c) is the cubic perovskite structure of BaMnO_3 with corner-sharing MnO_6 octahedra. This structure is referred to as “cubic.” Figure 10(d) is a tetragonal perovskite structure of BaMnO_3 with Mn off-center displacements along the z direction. This structure is referred to as “tetragonal.” Figure 10(e) is an orthorhombic perovskite structure of BaMnO_3 with Mn off-center displacements in the xy plane. This structure is referred to as “orthorhombic.” We first use the PBE+ U + J method to calculate the total energies of these structures at zero pressure, which are presented in Table II. We consider ferromagnetic and antiferromagnetic states (the spin arrangement for the antiferromagnetic state for each structure is explicitly shown as orange arrows in Fig. 10). The zero of energy is chosen as the energy of the antiferromagnetic state of the $2H$ structure, which has the lowest total energy among all the structures considered. We find that at ambient pressure all the perovskite structures of BaMnO_3 are about 0.7 eV/Mn higher in energy than the $2H$ structure. For each structure we also calculate the ferromagnetic-antiferromagnetic energy difference $\Delta E = E(\text{AF}) - E(\text{F})$. We see that without Mn off-center displacement ($2H$, $4H$, and cubic structures), the antiferromagnetic state has lower energy than the ferromagnetic state. With Mn off-center displacements (tetragonal and orthorhombic structures), the ferromagnetic state has lower energy. This further indicates that Mn off-center displacements help stabilize ferromagnetism. We also calculate the volume per Mn atom of each structure. We notice that antiferromagnetic state of the cubic structure has the smallest volume 61.9 \AA^3 per Mn, while the antiferromagnetic $2H$ structure that has the lowest total energy has a much larger volume 71.0 \AA^3 . Face-sharing oxygen octahedra are in fact more closely

packed than corner-sharing oxygen octahedra. However, in the $2H$ structure, between the “column” of face-sharing oxygen octahedra there is hollow space, which increases the volume.

The volume comparison suggests that external pressure can stabilize the cubic perovskite structure over the hexagonal $2H$ structure. To test this hypothesis, we calculate the total enthalpy as well as total energy of the antiferromagnetic $2H$ structure and antiferromagnetic cubic structure. The enthalpy difference $\Delta H = H(2H) - H(\text{cubic})$ and the energy difference $\Delta E = E(2H) - E(\text{cubic})$ are shown in Fig. 11(a). We find that at a critical pressure of 20 GPa, there is a transition from the $2H$ structure to the cubic structure. Compared to the energy difference ΔE , we can clearly see that it is the volume difference $\Delta V = V(2H) - V(\text{cubic})$ that stabilizes the cubic structure via pressure. A 20 GPa pressure is experimentally achievable and has been applied on cubic SrMnO_3 [29]. To make the discussion complete, we present in Fig. 11(b) the volume per Mn of the $2H$ structure and of the cubic structure as a function of pressure. We see that because the $2H$ structure is more hollow than the cubic structure, it is more compressible (the volume decreases faster with pressure). However, up to the critical pressure, the volume of the $2H$ structure is always larger than that of the cubic structure, which results in the pressure-driven structural transition. We need a few comments here: (i) we verified that with the application of pressure, there is no magnetic transition for the $2H$ structure and the cubic structure, i.e., the antiferromagnetic ordering always has lower energy than the ferromagnetic ordering; (ii) at the critical pressure, the Mn off-center displacements are suppressed, i.e., the tetragonal and orthorhombic perovskite

TABLE II. Total energies E with the zero point chosen as the total energy of $2H$ structure with antiferromagnetic ordering $\Delta E = E(\text{AF}) - E(\text{F})$, the energy difference between ferromagnetic ordering and antiferromagnetic ordering for each structure, and equilibrium volume Ω per Mn atom, calculated using the PBE+ U + J method with $U = 5 \text{ eV}$ and $J = 0.7 \text{ eV}$.

Structure	$2H$		$4H$		cubic		tetragonal		orthorhombic	
	FM	AFM	FM	AFM	FM	AFM	FM	AFM	FM	AFM
E (meV/Mn)	103	0	186	109	837	775	724	746	727	754
ΔE (meV/Mn)	-103		-77		-62		22		27	
Volume Ω ($\text{\AA}^3/\text{Mn}$)	71.6	71.0	66.4	66.1	62.9	61.9	65.9	64.1	65.8	63.4

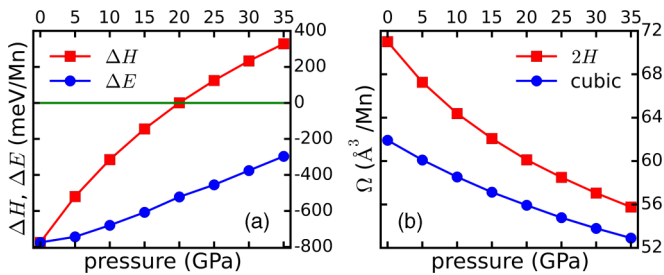


FIG. 11. Pressure dependence of the $2H$ structure and the cubic structure. For the $2H$ structures, we study the antiferromagnetic state; for the cubic structure, we study the G -type antiferromagnetic state. The results are calculated using the $PBE+U+J$ method with $U = 5$ eV and $J = 0.7$ eV. (a) Enthalpy difference between the $2H$ structure and the cubic structure $\Delta H = H(2H) - H(\text{cubic})$ (red curves). Energy difference between the $2H$ structure and the cubic structure $\Delta E = E(2H) - E(\text{cubic})$ (blue curves). The green line highlights the structural transition point. (b) Volume Ω per Mn atom of the $2H$ structure (red curves) and the cubic structure (blue curves).

structures are reduced to the cubic structure; and (iii) we repeated all the calculations using the sPBEsol and sPBE methods and find all the results are qualitatively consistent with a critical pressure of 21 GPa for sPBEsol and 25 GPa for sPBE.

VI. CONCLUSIONS

We have systematically studied the phase diagram of perovskite $\text{Sr}_{1-x}\text{Ba}_x\text{MnO}_3$ ($0 \leq x \leq 1$) as a function of Ba concentration x and epitaxial strain, as well as the phase diagram of hexagonal polymorphs of BaMnO_3 as a function of external pressure.

For perovskite $\text{Sr}_{1-x}\text{Ba}_x\text{MnO}_3$, we find that both increasing the Ba concentration and imposing epitaxial strain tend to stabilize a ferromagnetic-ferroelectric state. In the vicinity

of the phase boundary between a ferromagnetic state with a larger polarization and an antiferromagnetic state with a smaller polarization, either applying a magnetic field or an electric field can induce a first-order phase transition in polarization or magnetization, and thus realize an effective giant magnetoelectric coupling. However, the details of the phase diagram, in particular the critical Ba doping and critical epitaxial strain, strongly depend on the choice of exchange correlation functional. We find that among the three flavors of PBE exchange correlation functionals (sPBEsol, $PBE+U+J$, and $sPBE+U_{\text{eff}}$), sPBEsol least favors the ferromagnetism and predicts the largest critical Ba concentration and largest critical strain, while $sPBE+U_{\text{eff}}$ most favors the ferromagnetism and therefore predicts the smallest critical Ba concentration and smallest critical epitaxial strain (above some Ba concentration, epitaxial strain is not even needed to stabilize the ferromagnetic-ferroelectric state). We also show that a high pressure of over 20 GPa can stabilize the perovskite structure of BaMnO_3 over its hexagonal polymorphs.

Perovskite $\text{Sr}_{1-x}\text{Ba}_x\text{MnO}_3$ with $x > 0.5$ has not yet been synthesized in bulk or grown in thin film form [7]. We hope that our theoretical predictions on multiferroic properties of perovskite $\text{Sr}_{1-x}\text{Ba}_x\text{MnO}_3$ could stimulate further experiments.

ACKNOWLEDGMENTS

H. Chen is supported by National Science Foundation under Grant No. DMR-1120296. A. J. Millis is supported by National Science Foundation under Grant No. DMR-1308236. A. J. Millis thanks the College de France for hospitality and a stimulating intellectual environment while this paper was being prepared. Computational facilities are provided via Extreme Science and Engineering Discovery Environment (XSEDE), through Award No. TGPHY130003 and via the National Energy Research Scientific Computing Center (NERSC).

-
- [1] W. Eerenstein, N. D. Mathur, and J. F. Scott, *Nature (London)* **442**, 759 (2006).
- [2] R. Ramesh and N. A. Spaldin, *Nat. Mater.* **6**, 21 (2007).
- [3] J. Hong, A. Stroppa, J. Íñiguez, S. Picozzi, and D. Vanderbilt, *Phys. Rev. B* **85**, 054417 (2012).
- [4] H. Sakai, J. Fujioka, T. Fukuda, D. Okuyama, D. Hashizume, F. Kagawa, H. Nakao, Y. Murakami, T. Arima, A. Q. R. Baron *et al.*, *Phys. Rev. Lett.* **107**, 137601 (2011).
- [5] G. Giovannetti, S. Kumar, C. Ortix, M. Capone, and J. van den Brink, *Phys. Rev. Lett.* **109**, 107601 (2012).
- [6] R. Nourafkan, G. Kotliar, and A.-M. S. Tremblay, *Phys. Rev. B* **90**, 220405 (2014).
- [7] E. Langenberg, R. Guzmán, L. Maurel, L. M. de Baos, L. Morelln, M. R. Ibarra, J. Herrero-Martín, J. Blasco, C. Magn, P. A. Algarabel *et al.*, *ACS Appl. Mater. Interfaces* **7**, 23967 (2015).
- [8] D. K. Pratt, J. W. Lynn, J. Mais, O. Chmaissem, D. E. Brown, S. Kolesnik, and B. Dabrowski, *Phys. Rev. B* **90**, 140401 (2014).
- [9] J. M. Rondinelli, A. S. Eidelson, and N. A. Spaldin, *Phys. Rev. B* **79**, 205119 (2009).
- [10] J. H. Lee and K. M. Rabe, *Phys. Rev. Lett.* **104**, 207204 (2010).
- [11] C. J. Fennie and K. M. Rabe, *Phys. Rev. Lett.* **97**, 267602 (2006).
- [12] H. Chen and A. J. Millis, *Phys. Rev. B* **93**, 205110 (2016).
- [13] P. Hohenberg and W. Kohn, *Phys. Rev.* **136**, B864 (1964).
- [14] W. Kohn and L. J. Sham, *Phys. Rev.* **140**, A1133 (1965).
- [15] M. C. Payne, M. P. Teter, D. C. Allan, T. A. Arias, and J. D. Joannopoulos, *Rev. Mod. Phys.* **64**, 1045 (1992).
- [16] G. Kresse and J. Furthmüller, *Phys. Rev. B* **54**, 11169 (1996).
- [17] P. E. Blöchl, *Phys. Rev. B* **50**, 17953 (1994).
- [18] G. Kresse and D. Joubert, *Phys. Rev. B* **59**, 1758 (1999).
- [19] J. P. Perdew, K. Burke, and M. Ernzerhof, *Phys. Rev. Lett.* **77**, 3865 (1996).
- [20] A. I. Liechtenstein, V. I. Anisimov, and J. Zaanen, *Phys. Rev. B* **52**, R5467(R) (1995).
- [21] J. P. Perdew, A. Ruzsinszky, G. I. Csonka, O. A. Vydrov, G. E. Scuseria, L. A. Constantin, X. Zhou, and K. Burke, *Phys. Rev. Lett.* **100**, 136406 (2008).

- [22] R. D. King-Smith and D. Vanderbilt, *Phys. Rev. B* **47**, 1651 (1993).
- [23] J. Y. Jo, Y. S. Kim, T. W. Noh, J.-G. Yoon, and T. K. Song, *Appl. Phys. Lett.* **89**, 232909 (2006).
- [24] H. Chen and A. J. Millis, *Phys. Rev. B* **93**, 045133 (2016).
- [25] J. H. Lee, L. Fang, E. Vlahos, X. Ke, Y. W. Jung, L. F. Kourkoutis, J.-W. Kim, P. J. Ryan, T. Heeg, M. Roeckerath *et al.*, *Nature (London)* **466**, 954 (2010).
- [26] The slight difference between our results and Ref. [10] is because our critical strain is extracted from calculations of *Amm2* symmetry with polarization along the [110] direction while in Ref. [10] the critical strain is extracted from calculations of *Ima2* symmetry.
- [27] R. Søndena, S. Stølen, P. Ravindran, T. Grande, and N. L. Allan, *Phys. Rev. B* **75**, 184105 (2007).
- [28] R. Søndena, P. Ravindran, S. Stølen, T. Grande, and M. Hanfland, *Phys. Rev. B* **74**, 144102 (2006).
- [29] M. B. Nielsen, D. Ceresoli, P. Parisiades, V. B. Prakapenka, T. Yu, Y. Wang, and M. Bremholm, *Phys. Rev. B* **90**, 214101 (2014).